Photovoltaic Devices

International Edition: DOI: 10.1002/anie.201505882
German Edition: DOI: 10.1002/ange.201505882

Controllable Growth of Perovskite Films by Room-Temperature Air Exposure for Efficient Planar Heterojunction Photovoltaic Cells

*Bin Yang, Ondrej Dyck, Jonathan Poplawsky, Jong Keum, Sanjib Das, Alexander Puretzky, Tolga Aytug, Pooran C. Joshi, Christopher M. Rouleau, Gerd Duscher, David B. Geohegan, and Kai Xiao**

Abstract: *A two-step solution processing approach has been established to grow void-free perovskite films for low-cost high-performance planar heterojunction photovoltaic devices. A high-temperature thermal annealing treatment was applied to drive the diffusion of CH_3NH_3I precursor molecules into a compact PbI_2 layer to form perovskite films. However, thermal annealing for extended periods led to degraded device performance owing to the defects generated by decomposition of perovskite into PbI_2. A controllable layer-by-layer spin-coating method was used to grow "bilayer" CH_3NH_3I/PbI_2 films, and then drive the interdiffusion between PbI_2 and CH_3NH_3I layers by a simple air exposure at room temperature for making well-oriented, highly crystalline perovskite films without thermal annealing. This high degree of crystallinity resulted in a carrier diffusion length of ca. 800 nm and a high device efficiency of 15.6 %, which is comparable to values reported for thermally annealed perovskite films.*

Low-cost organometal halide perovskite solar cells have emerged as a prime candidate to meet the future energy generation demands on a gigawatt scale, owing to the certified power conversion efficiency (PCE) of around 20 % with simple solution-based processing approaches.[1–5] One-step solution-based approaches to grow hybrid perovskite thin films have typically generated a large density of pinholes or voids within perovskite films,[6,7] which adversely impact the photovoltaic performance, especially in planar heterojunction configuration devices. Furthermore, large variations in film morphology significantly limited device performance reliability, impacting yield.[8,9] As a result, two-step solution-based processing techniques such as methylammonium iodide (CH_3NH_3I) vapor assistance[10] and the lead iodide (PbI_2)/CH_3NH_3I bilayer interdiffusion.[11–13] have been developed to grow void-free perovskite thin films.[10–14] These approaches employ high temperature (for example, ≥ 100 °C) thermal annealing to drive the diffusion of CH_3NH_3I precursor molecules into the dense PbI_2 layer to form compact methylammonium lead triiodide ($CH_3NH_3PbI_3$) perovskite thin films. However, thermal annealing for extended periods is known to cause the decomposition of perovskites into PbI_2, which degrades the device performance by acting as defects in the perovskite thin films.[15] Therefore, finding simple and reliable solution processing approaches for void-free and highly crystalline perovskite films for efficient solar cells without thermal annealing is highly desirable for practical solar-cell manufacturing technology.

Herein we report a simple room-temperature, air-exposure process that removes the thermal annealing step and drives the interdiffusion of PbI_2 and CH_3NH_3I layers to synthesize highly crystalline and pinhole-free $CH_3NH_3PbI_3$ perovskite films. The interdiffusion process and the resulting formation of $CH_3NH_3PbI_3$ films were characterized by in situ X-ray diffraction (XRD), which revealed that ambient water molecules are a driving force for the interdiffusion. Perovskite thin-film photovoltaic devices resulting from the new air-exposure process displayed a PCE of 15.6 %, which is comparable to that of most thermally annealed perovskite devices.

The PbI_2 layer and CH_3NH_3I layer were spin-coated sequentially onto TiO_2/ITO glass substrates using dimethylformamide (DMF) and 2-propanol, respectively. As shown in Figure 1 a, the initial as-cast "bilayer" thin film not only exhibits Bragg peaks associated with PbI_2 crystal (001) planes at 12.54°, but also strong $CH_3NH_3PbI_3$ peaks at 14.05° and at 28.37° for the (110) and (220) planes, respectively, indicating the formation of perovskite crystals resulting from the CH_3NH_3I spin-coating process. It should be noted that another peak appeared at 13.89°, which was indexed as the perovskite $CH_3NH_3PbI_3$ (002) plane using Rietveld analysis (Supporting Information, Figure S1). Therefore, this initial stage of the as-cast film can be viewed as a "trilayer" film with a layer of $CH_3NH_3PbI_3$ perovskite crystals sandwiched between PbI_2 and CH_3NH_3I precursor layers (Figure 1 b). The as-cast $PbI_2/CH_3NH_3PbI_3/CH_3NH_3I$ "trilayer" films were exposed to ambient air at room temperature with a humidity of about 30 %. After 60 min, the PbI_2 precursors were found to have completely converted into $CH_3NH_3PbI_3$ perovskites,

---

[*] B. Yang, J. Poplawsky, J. Keum, A. Puretzky, C. M. Rouleau,
D. B. Geohegan, K. Xiao
Center for Nanophase Materials Sciences
Oak Ridge National Laboratory, Oak Ridge, TN, 37831 (USA)
E-mail: xiaok@ornl.gov

O. Dyck, G. Duscher
Department of Materials Science and Engineering
University of Tennessee, Knoxville, TN, 37996 (USA)

S. Das
Department of Electrical Engineering and Computer Science
University of Tennessee, Knoxville, TN, 37996 (USA)

T. Aytug
Chemical Sciences Division
Oak Ridge National Laboratory, Oak Ridge, TN 37831 (USA)

P. C. Joshi
Materials Science and Technology Division
Oak Ridge National Laboratory, Oak Ridge, TN 37831 (USA)

Supporting information for this article is available on the WWW under http://dx.doi.org/10.1002/anie.201505882.

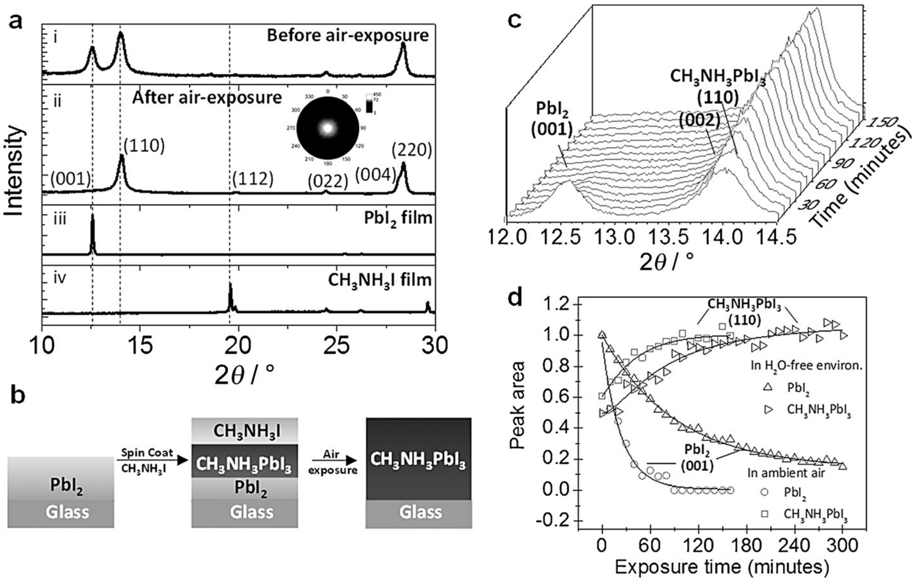

Figure 1. a) X-ray diffraction pattern of an as-cast glass/PbI_2/CH_3NH_3I film before air exposure (i), after air-exposure for 60 min (ii), glass/PbI_2 film (iii), and glass/CH_3NH_3I film (iv). Inset: X-ray pole figure acquired from the [110] direction for the air-exposure perovskite film. b) Depiction of the perovskite thin film growth process. c) Evolution of the X-ray diffraction pattern as a function of ambient air-exposure time by monitoring peaks at 12.54° (the (001) plane of PbI_2), 13.89° (the (002) plane of $CH_3NH_3PbI_3$), and 14.05° (the (110) plane of $CH_3NH_3PbI_3$). d) A comparison of the PbI_2 (001) plane and the $CH_3NH_3PbI_3$ (110) plane peak areas as a function of exposure time for the air and water-free environment.

as indicated by the disappearance of the PbI_2 (001) Bragg peak (Figure 1 a). X-ray pole figures were used to probe the global orientation and crystallographic texture of such films, and Figure 1 a indicates that they were well-oriented with the $CH_3NH_3PbI_3$ (110) planes parallel to the surface of the substrate. Note that this plane has been theoretically identified as the most stable surface in the tetragonal phase of $CH_3NH_3PbI_3$.[16] The SEM image shows that the $CH_3NH_3PbI_3$ perovskite film is free of pinholes, although a few large (ca. 1 μm) "flower-like" perovskite crystals are observed (Supporting Information, Figure S2). Atomic force microscopy was used to understand the surface roughness of the film and the large "flower-like" crystals. The root-mean-square roughness of a 20 μm × 20 μm area on an air-exposed film was about 34 nm, and the large "flower-like" crystals (Supporting Information, Figure S2) have an average height of 70 nm, indicating they protrude above the surface of the film.

To investigate the evolution of the perovskite phase in the as-cast thin films during ambient exposure, in situ X-ray diffraction was employed to monitor the PbI_2 (001) and $CH_3NH_3PbI_3$ (110) Bragg peaks as a function of time. As shown in Figure 1 c, with increasing exposure time, the PbI_2 Bragg peak gradually decreased while the $CH_3NH_3PbI_3$ Bragg peak simultaneously increased (Figure 1 c,d), indicating the PbI_2 and CH_3NH_3I precursors were reacting to grow the $CH_3NH_3PbI_3$ crystals. After 60 min of exposure, the PbI_2 peak completely disappeared, and the intensity of the $CH_3NH_3PbI_3$ (110) peak correspondingly stabilizes, indicating that the reaction and crystallization were complete. To understand whether humidity was the driving force for the interdiffusion, air exposure studies were conducted on a similar initial PbI_2/$CH_3NH_3PbI_3$/CH_3NH_3I "trilayer" film at room temperature in a water-free chamber ($H_2O <$ 0.1 ppm). Interestingly, despite an essentially dry environment, the peak area intensity of the PbI_2 (001) plane was again found to decrease and the peak intensity of the $CH_3NH_3PbI_3$ (110) plane correspondingly increased, however more slowly (Supporting Information, Figure S3). This suggests that PbI_2 and CH_3NH_3I can gradually convert into $CH_3NH_3PbI_3$ even in a water-free environment, although at a much lower rate as shown in Figure 1 d. It is thus hypothesized that ambient water accelerates the chemical reaction between PbI_2 and CH_3NH_3I owing to the existence of a more reactive and metastable $CH_3NH_3PbI_3{\cdot}H_2O$ phase, which then spontaneously releases its water molecules at room temperature.[17,18]

To assess the applicability of the films for solar cells, prototype devices were fabricated. We first examined the photovoltaic performance of electron transporting layer (ETL)-free devices (ITO/$CH_3NH_3PbI_3$/2,2′,7,7′-tetrakis-(N,N-di-pmethoxyphenylamine)-9,9′-spirobifluorene (Spiro-OMeTAD)/Ag) based on our air-exposed perovskite films. To grow compact perovskite layers, a UV–ozone treatment for 10 min was used to generate a hydrophilic ITO glass surface, as shown by water contact-angle measurements (Supporting Information, Figure S4). Surprisingly, when swept from forward bias to reverse bias, the device without TiO_2 yielded a J_{SC} of 18.7 mA cm^{-2}, a V_{OC} of 1.02 V, a FF of 72 %, and a PCE of 13.8 % (Figure 2 a). The cross-sectional SEM image acquired from such a high-performance TiO_2-free device shows a compact perovskite layer (Supporting Information, Figure S5), which is consistent with previous results.[7] To verify the J_{SC} from the J–V curve, the external quantum efficiencies (EQEs) were measured (Supporting Information, Figure S6). By integrating the EQE curve across the standard AM 1.5 G solar spectrum (100 mA cm^{-2}), a J_{SC} of 18.2 mA cm^{-2} was calculated, which is consistent with the J_{SC} measured from the J–V scan. For comparison, a TiO_2 ETL was incorporated into the devices, and as shown in Figure 2 a, the typical device exhibited improved performance; that is, a J_{SC} of 19.8 mA cm^{-2}, a V_{OC} of 1.03 V, a high FF of 76 %, and a PCE of 15.6 % when swept from forward bias to reverse bias. It should be noted that both types of devices, with and without TiO_2, exhibited hysteresis characteristics as shown in the Supporting Information, Figure S7. To reveal how the J–V hysteresis affects the maximum power output from our devices, we measured a device in both forward and reverse scan mode, which showed PCEs of 15.2 % and 8 %, respectively (Supporting Information, Figure S7). We then acquired

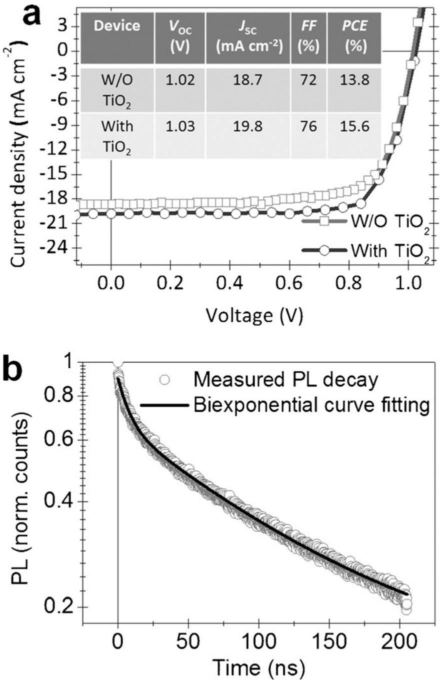

Figure 2. a) Comparison of *J*–*V* curves of devices without (□) and with (○) TiO$_2$ acquired under standard illumination (AM 1.5 G, 100 mW cm^{-2}). The obtained photovoltaic parameters are shown in the inset table. b) Time-resolved photoluminescence (PL) at about 760 nm (○), showing a biexponential decay characteristic (——).

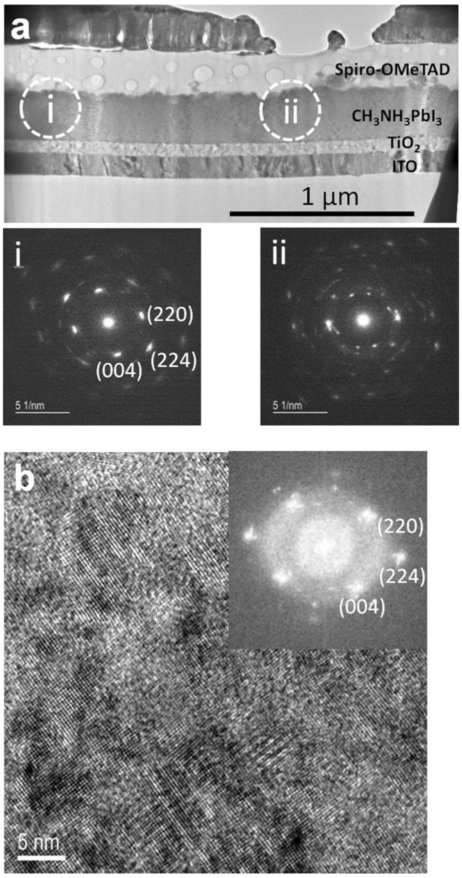

Figure 3. a) Bright-field cross-sectional TEM image of an entire device with a TiO$_2$ layer. Two typical SAED patterns (i and ii) were acquired from CH$_3$NH$_3$PbI$_3$ layer. Pattern i shows identical crystallographic orientation, whereas pattern ii shows multiple grain orientations within the aperture diameter size of 325 nm. b) High-resolution TEM image taken from the CH$_3$NH$_3$PbI$_3$ layer. Inset: the corresponding FFT pattern, viewed along the [110] zone axis. Note that indexing of the (004) and (220) diffraction spots could possibly be switched, because the similar d spacing prevents unambiguous determination of these spot locations.

the photocurrent as a function of time measured at the maximum power output point (0.792 V) under an illumination of 100 mW cm^{-2}. The photocurrent density saturated at about 16 mA cm^{-2}, and the device showed a stable PCE of about 12.7 %, despite the strong *J*–*V* hysteresis.

To further understand the origin of their high photovoltaic performance, we first characterized the time-resolved photoluminescence (PL) at about 760 nm (Figure 2 b). Based on the biexponential fitting results, two lifetimes were obtained: a short lifetime of 8.3 ns and a long lifetime of 114.2 ns. The fast decay is ascribed to significant surface recombination, while the slow decay is attributed to the dominant free carrier decay within the bulk film.[19] Hall measurements of the air-exposed perovskite films showed a carrier mobility of about 2.16 cm^2 V^{-1} s^{-1} (Supporting Information, Figure S8), and when combined with carrier lifetime measured previously, the carrier diffusion length was estimated to be about 800 nm, which is comparable to the carrier diffusion length in most thermally annealed CH$_3$NH$_3$PbI$_3$ perovskite thin films.[13] Therefore, the high photovoltaic performance for both types of air-exposed perovskite film devices (with and without TiO$_2$) should be partially attributed to this long carrier diffusion length.

To understand the cross-sectional morphology and crystallinity of the devices, cross-sectional TEM images and SAED studies were performed. In Figure 3 a, the compact CH$_3$NH$_3$PbI$_3$ perovskite layer was clearly identified in the cross-sectional TEM image of our high performance device, which has an ITO/TiO$_2$/CH$_3$NH$_3$PbI$_3$/Spiro-OMeTAD/Ag architecture (Figure 3 a). A series of SAED patterns were acquired along the direction parallel to the glass substrate to examine the crystallographic features of the perovskite film. Two typical SAED patterns are shown in Figure 3 a. We observed a polycrystalline spot pattern (pattern i) with each domain oriented very similarly over a distance of 325 nm (the aperture diameter), suggesting a preferential growth direction, which is consistent with a preferred crystal orientation of [110] as revealed by X-ray pole figure measurements. Pattern i is consistent with previously reported observations where CH$_3$NH$_3$PbI$_3$ is viewed along the [110] zone axis.[20] However, it should be noted that we also observed regions where the crystals did not orient similarly, as shown by pattern ii. A high-resolution TEM image (Figure 3 b) and the corresponding fast Fourier transform (FFT; inset of Figure 3 b) were taken from the ambient-air-exposed perovskite layer, and clear lattice fringes and a well-ordered crystal lattice were observed, despite the presence of surface damage owing to focused-ion beam milling during sample preparation. Thus, it is concluded that the high crystallinity and highly oriented nature of the perovskite layer contributes significantly to the long carrier diffusion in ambient-air-exposure perovskite thin films.

Electron-beam-induced current (EBIC) measurements were employed to further investigate the device operation mechanism. The cross-sectional SEM and corresponding EBIC images are shown in Figure 4a. The line profiles of the SEM and corresponding EBIC were taken across the entire device, as indicated in Figure 4b. The EBIC signal was only observed within the $CH_3NH_3PbI_3$ perovskite layer, indicating that the perovskite layer is the only layer generating free charge carriers that can be collected by the electrodes. A uniform carrier generation was observed in the perovskite film with slight peaks close to the perovskite/TiO_2 and perovskite/Spiro-OMeTAD inherent for a *p*-i-n structure.

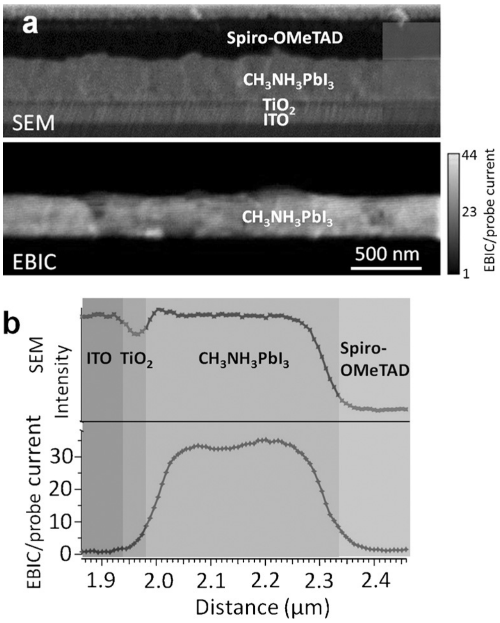

Figure 4. a) SEM (top) and EBIC (bottom) images of a device with a TiO_2 layer, with the corresponding average line profiles shown in (b). The line profiles in (b) were taken in the region displayed in (a).

In summary, a simple room-temperature air-exposure approach was developed to grow highly crystalline, well-oriented perovskite films, resulting in a long carrier diffusion length of about 800 nm. The devices with and without TiO_2 ETL yielded PCEs of 15.6% and 13.8%, respectively, which are comparable to those of most thermally annealed perovskite devices. The non-thermal-annealing, room-temperature air-exposure approach is compatible with roll-to-roll processing, which enables very low-cost flexible photovoltaics.

Acknowledgements

This research was conducted at the Center for Nanophase Materials Sciences (CNMS), which is a DOE Office of Science User Facility.

Keywords: air exposure · in situ X-ray diffraction · perovskites · photovoltaic devices · thin films

How to cite: *Angew. Chem. Int. Ed.* **2015**, *54*, 14862–14865
Angew. Chem. **2015**, *127*, 15075–15078

[1] J. Burschka, N. Pellet, S.-J. Moon, R. Humphry-Baker, P. Gao, M. K. Nazeeruddin, M. Gratzel, *Nature* **2013**, *499*, 316–319.
[2] S. Das, B. Yang, G. Gu, P. C. Joshi, I. N. Ivanov, C. M. Rouleau, T. Aytug, D. B. Geohegan, K. Xiao, *ACS Photonics* **2015**, *2*, 680–686.
[3] F. Hao, C. C. Stoumpos, D. H. Cao, R. P. H. Chang, M. G. Kanatzidis, *Nat. Photonics* **2014**, *8*, 489–494.
[4] N. J. Jeon, J. H. Noh, W. S. Yang, Y. C. Kim, S. Ryu, J. Seo, S. I. Seok, *Nature* **2015**, *517*, 476–480.
[5] B. Yang, O. Dyck, J. Poplawsky, J. Keum, A. Puretzky, S. Das, I. N. Ivanov, C. Rouleau, G. Duscher, D. B. Geohegan, K. Xiao, *J. Am. Chem. Soc.* **2015**, *137*, 9210–9213.
[6] G. E. Eperon, V. M. Burlakov, P. Docampo, A. Goriely, H. J. Snaith, *Adv. Funct. Mater.* **2014**, *24*, 151–157.
[7] W. Ke, G. Fang, J. Wan, H. Tao, Q. Liu, L. Xiong, P. Qin, J. Wang, H. Lei, G. Yang, M. Qin, X. Zhao, Y. Yan, *Nat. Commun.* **2015**, *6*, DOI: 10.1038/ncomms7700.
[8] B. Conings, L. Baeten, C. De Dobbelaere, J. D'Haen, J. Manca, H.-G. Boyen, *Adv. Mater.* **2014**, *26*, 2041–2046.
[9] W. Zhang, M. Saliba, D. T. Moore, S. K. Pathak, M. T. Hörantner, T. Stergiopoulos, S. D. Stranks, G. E. Eperon, J. A. Alexander-Webber, A. Abate, A. Sadhanala, S. Yao, Y. Chen, R. H. Friend, L. A. Estroff, U. Wiesner, H. J. Snaith, *Nat. Commun.* **2015**, *6*, DOI: 10.1038/ncomms7142.
[10] Q. Chen, H. Zhou, Z. Hong, S. Luo, H.-S. Duan, H.-H. Wang, Y. Liu, G. Li, Y. Yang, *J. Am. Chem. Soc.* **2014**, *136*, 622–625.
[11] C.-W. Chen, H.-W. Kang, S.-Y. Hsiao, P.-F. Yang, K.-M. Chiang, H.-W. Lin, *Adv. Mater.* **2014**, *26*, 6647–6652.
[12] Y. Chen, T. Chen, L. Dai, *Adv. Mater.* **2015**, *27*, 1053–1059.
[13] Z. Xiao, Q. Dong, C. Bi, Y. Shao, Y. Yuan, J. Huang, *Adv. Mater.* **2014**, *26*, 6503–6509.
[14] J.-H. Im, I.-H. Jang, N. Pellet, M. Grätzel, N.-G. Park, *Nat. Nanotechnol.* **2014**, *9*, 927–932.
[15] C. Bi, Y. Shao, Y. Yuan, Z. Xiao, C. Wang, Y. Gao, J. Huang, *J. Mater. Chem. A* **2014**, *2*, 18508–18514.
[16] J. Haruyama, K. Sodeyama, L. Han, Y. Tateyama, *J. Phys. Chem. Lett.* **2014**, *5*, 2903–2909.
[17] F. Hao, C. C. Stoumpos, Z. Liu, R. P. Chang, M. G. Kanatzidis, *J. Am. Chem. Soc.* **2014**, *136*, 16411–16419.
[18] H. Zhou, Q. Chen, G. Li, S. Luo, T.-b. Song, H.-S. Duan, Z. Hong, J. You, Y. Liu, Y. Yang, *Science* **2014**, *345*, 542–546.
[19] D. Shi, V. Adinolfi, R. Comin, M. Yuan, E. Alarousu, A. Buin, Y. Chen, S. Hoogland, A. Rothenberger, K. Katsiev, Y. Losovyj, X. Zhang, P. A. Dowben, O. F. Mohammed, E. H. Sargent, O. M. Bakr, *Science* **2015**, *347*, 519–522.
[20] H. Zhu, Y. Fu, F. Meng, X. Wu, Z. Gong, Q. Ding, M. V. Gustafsson, M. T. Trinh, S. Jin, X. Zhu, *Nat. Mater.* **2015**, *14*, 636–642.

Received: June 29, 2015
Revised: October 21, 2015